

Spin-wave damping in ferromagnetic stripes with inhomogeneous magnetization

Hoa T. Nguyen, A. Akbari-Sharbat, and M. G. Cottam

Department of Physics & Astronomy, University of Western Ontario, London, Ontario, Canada N6A 3K7

(Received 15 February 2011; published 16 June 2011)

A theory is presented for the interactions between the dipole-exchange spin waves in ferromagnetic nanowires with a stripe geometry. A Hamiltonian-based approach is used in order to extend earlier results for the linear (or noninteracting) spin waves to include the leading nonlinear processes due to three-magnon and four-magnon effects in a stripe. As well as the magnetic dipole-dipole and exchange terms in the Hamiltonian, the role of an applied magnetic field that can be either parallel or perpendicular to the stripe axis is considered. Within a diagrammatic perturbation method the contributions to the frequency shift and damping of the quantized spin waves are deduced. Numerical calculations are presented for Permalloy stripes, and it is shown that the damping in the transverse field case, where the magnetization may become strongly inhomogeneous, can be larger than that in the longitudinal field case. Comparisons are made with recent damping measurements for Permalloy stripes in a longitudinal field.

DOI: [10.1103/PhysRevB.83.214423](https://doi.org/10.1103/PhysRevB.83.214423)

PACS number(s): 75.30.Ds, 75.40.Gb, 75.75.-c, 75.78.-n

I. INTRODUCTION

Ferromagnetic nanowires, grown either individually or in dense arrays, have been intensively studied in recent years (for reviews, see e.g., Refs. 1–3). In particular, the spin-wave dynamics in these confined geometries has been investigated experimentally by various techniques that include Brillouin light scattering,^{4–8} the spatially resolved Kerr method,⁹ ferromagnetic resonance,^{10,11} etc. On the theoretical side the lateral confinement of spin waves in nanowires (e.g., in dealing with the lateral edges in magnetic stripes) presents challenging problems, but there has been considerable progress regarding the *linear* spin-wave dynamics. Broadly, two approaches have been followed, of which one is a macroscopic (or continuum) approach based on solving simultaneously the Landau-Lifshitz-Gilbert equation of motion of the magnetization and Maxwell's equations for the magnetic-field components with appropriate boundary conditions (see e.g., Ref. 12). As discussed by Guslienko and Slavin,¹³ it is necessary to introduce effective boundary conditions with the pinning parameters usually chosen phenomenologically in order to deal with regions of strong spatial inhomogeneity in the magnetization, such as at the lateral edges of a stripe. The other approach is based on a microscopic technique^{14,15} in which a spin Hamiltonian describing the exchange and magnetic dipole-dipole interactions is employed, together with terms for an applied magnetic field and any single-ion anisotropy. It involves introducing a lattice of effective spins, with the lattice parameter chosen to be small compared with the so-called exchange length of the material (see Ref. 14), e.g., about 5.3 nm in Permalloy. The surface pinning arises in this theory because the total effective dipole fields have a position dependence and the regions of spatial inhomogeneities can be explicitly taken into account.

In this paper we are concerned with extending the above theory of linear spin waves in magnetic nanowires to take account of nonlinear processes in the spin dynamics. This is done within the context of the microscopic approach applied to ferromagnetic stripes, which we use to derive results for the frequency shift and damping of the spatially quantized spin waves as a generalization of Ref. 15 for the linear (or

noninteracting) spin waves. Our calculations are motivated in part by recent ferromagnetic resonance (FMR) experiments reported for spin waves in Permalloy stripes¹¹ where damping effects were observed. Numerical applications will therefore be made to Permalloy stripes, taking the same stripe width and thickness as in some of the experiments. Our theory covers the two different cases of an external magnetic field applied either in the longitudinal direction along the stripe axis, as in the above experiments, or in the transverse direction. In the latter case, the magnetization is tilted away from the preferred longitudinal axis and is spatially inhomogeneous, which we will show leads to a larger damping under suitable conditions.

In our earlier study of linear spin waves in magnetic stripes¹⁵ a transformation of the Hamiltonian from spin operators to boson operators was made, with only the lowest-order terms being retained in an expansion. In the present work we also retain the higher-order terms that describe the three-magnon and four-magnon interaction terms for the wire geometry. It is well known from extensive previous studies of bulk materials and thin films (see e.g., Refs. 16–19) that these two types of terms are required for a proper description of nonlinear spin-wave processes, including spin-wave damping, spin-wave instabilities under strong pumping fields, nonlinear generation of spin waves, etc. Here we focus on applications to the spin-wave frequency shift and damping in order to make connections with the experimental data in Ref. 11. Specifically, we take account of the three- and four-magnon processes through a diagrammatic perturbation expansion by analogy with previous calculations for ultrathin ferromagnetic films.²⁰

This paper is organized as follows. In Sec. II we give an outline of the theoretical model, including the spin Hamiltonian and the assumed geometry of a ferromagnetic stripe. The extension of our earlier work for the linear spin-wave (SW) properties¹⁵ to include nonlinear SW effects through the three-magnon and four-magnon processes is then presented using a diagrammatic perturbation formalism. Expressions are derived for the corresponding frequency shift and damping for any SW branch, taking either a longitudinal or a transverse applied magnetic field. Numerical calculations are made in Sec. III for the longitudinal field case, emphasizing the behavior for

the SW damping in Permalloy stripes, as recently studied experimentally.¹¹ This is followed in Sec. IV by numerical calculations for the transverse field case showing that the SW damping may be significantly larger. Further discussion and the conclusions are given in Sec. V.

II. THEORY

Following our earlier work on the *linear* SW spectrum,¹⁵ a ferromagnetic striped nanowire will be modeled as having a rectangular cross section (in the xz plane) with width W and thickness L (where usually $W \gg L$), while the system is effectively infinite in the y direction (see Fig. 1). A lattice of spins is introduced, arranged on a simple cubic lattice, where the effective lattice constant a is chosen to be smaller than the exchange length of the material. The cross section of the wire has a finite number N of spins, where typical N values might be as large as several hundreds depending on W and L .

The system of interacting spins is described by the Hamiltonian

$$H = - \sum_{(i,j)} \sum_{\alpha,\beta} U_{ij}^{\alpha\beta} S_i^\alpha S_j^\beta - g\mu_B \mathbf{H}_0 \cdot \sum_i \mathbf{S}_i. \quad (1)$$

Here the indices i and j label the spin sites and α and β denote the Cartesian components x , y , or z . The first term includes both the short-range exchange and the long-range dipole-dipole interactions between spins \mathbf{S}_i and \mathbf{S}_j (with quantum number S), where the summations are over all distinct pairs of spins and

$$U_{ij}^{\alpha\beta} = -J_{ij}\delta_{\alpha\beta} + (g\mu_B)^2 \frac{|\mathbf{r}_{ij}|^2 \delta_{\alpha\beta} - 3r_{ij}^\alpha r_{ij}^\beta}{|\mathbf{r}_{ij}|^5}. \quad (2)$$

We consider the above exchange interactions J_{ij} to be nonzero only between the nearest neighbors, whereas the dipole-dipole part couples all spins (where $\mathbf{r}_{ij} = \mathbf{r}_j - \mathbf{r}_i$). The second term in the Hamiltonian Eq. (1) describes the Zeeman interaction of the spins with an external magnetic field of magnitude H_0 applied either parallel or perpendicular to the stripe length. A term to represent the single-ion anisotropy could straightforwardly be added but will be ignored for the applications to be considered in this paper. By using an expansion in terms of boson operators and a diagrammatic perturbation technique, we next investigate the nonlinear SW processes in ferromagnetic wires (the damping in particular) for the two directions of the external magnetic field.

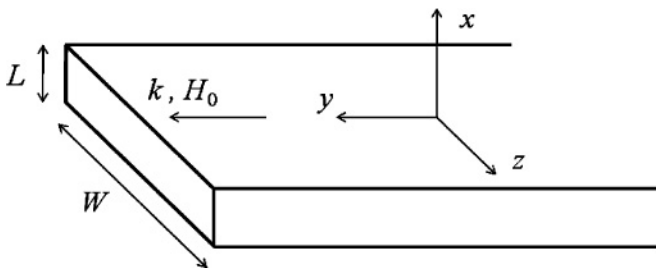


FIG. 1. Geometry of an infinitely long magnetic stripe of width W and thickness L , showing the choice of coordinate axes. The wave number along the y axis is k , and magnetic field H_0 is chosen to be either along the y axis (as illustrated) or along the z axis.

A. Longitudinal applied field

In this case, where the magnetic field is applied parallel to the stripe length as in the recent damping measurements¹¹ using FMR, the equilibrium configuration of all spins is along the y direction by symmetry. Then, as in Refs. 15 and 14, we may use the Holstein-Primakoff representation to rewrite the Hamiltonian in terms of boson creation and annihilation operators a_i^\dagger and a_i . The result may be expanded as

$$H = H^{(0)} + H^{(1)} + H^{(2)} + H^{(3)} + H^{(4)} + \dots, \quad (3)$$

where the general term $H^{(m)}$ consists of normal-ordered products of m boson operators. The zero-order term $H^{(0)}$ is just a constant while $H^{(1)}$ vanishes due to the symmetry in this longitudinal case. The second-order term $H^{(2)}$ describes the noninteracting (or linear) SW modes at low temperatures $T \ll T_C$ (where T_C is the Curie temperature) and has the form

$$H^{(2)} = \sum_{k,n,m} [A_{n,m}^{(2)}(k) a_{k,n}^\dagger a_{k,m} + B_{n,m}^{(2)}(k) a_{k,n}^\dagger a_{-k,m} + B_{n,m}^{(2)*}(k) a_{k,n} a_{-k,m}]. \quad (4)$$

Here k is a wave number along the stripe axis which arises when a Fourier transform is taken with respect to the y axis as the direction of translational symmetry. The integers n and m label the spin sites in each cross section of the stripe, taking the values $\{1, 2, \dots, N\}$, where N denotes the number of spin sites. Denoting $J_{n,m}(k)$ and $D_{n,m}^{\alpha\beta}(k)$ as the Fourier transforms with respect to k of the exchange and dipolar interactions, the coefficients $A_{n,m}^{(2)}$ and $B_{n,m}^{(2)}$ are

$$A_{n,m}^{(2)}(k) = \left\{ g\mu_B H_0 + S \sum_{p=1}^N [J_{n,p}(0) - (g\mu_B)^2 D_{n,p}^{yy}(0)] \right\} \delta_{n,m} - S J_{n,m}(k) - \frac{1}{2} S (g\mu_B)^2 D_{n,m}^{yy}(k), \quad (5)$$

$$B_{n,m}^{(2)}(k) = \frac{1}{4} S (g\mu_B)^2 \{ D_{n,m}^{zz}(k) - D_{n,m}^{xx}(k) + 2i D_{n,m}^{xz} \}. \quad (6)$$

The next terms $H^{(m)}$ (with $m \geq 3$) of the expansion in Eq. (3) describe the nonlinear SW dynamics in the nanowire. In general, it is well known (see e.g., Refs. 16, 18, and 19) that both the $H^{(3)}$ and $H^{(4)}$ terms, representing three-magnon and four-magnon processes, respectively, need to be included to account for the leading-order effects of the SW interactions. In the present case they are given by

$$H^{(3)} = \sum_{k,q,n,m} [A_{n,m}^{(3)}(k) a_{k,n}^\dagger a_{q,m}^\dagger a_{k+q,m} + A_{n,m}^{(3)*}(k) a_{q,n}^\dagger a_{q-k,n} a_{k,m}], \quad (7)$$

$$H^{(4)} = \sum_{k,k',q,n,m} \{ A_{n,m}^{(4)}(k) [a_{k,n}^\dagger a_{k',m}^\dagger a_{q,m} a_{k+k'-q,m} + a_{q,n}^\dagger a_{k',n}^\dagger a_{k,m} a_{-k+k'+q,n}] + B_{n,m}^{(4)}(k) a_{q,m}^\dagger a_{k',n}^\dagger a_{-k+k',n} a_{k+q,m} + C_{n,m}^{(4)}(k) a_{-k,m}^\dagger a_{k',n}^\dagger a_{q,n}^\dagger a_{-k+k'+q,n} + C_{n,m}^{(4)*}(k) a_{k',n}^\dagger a_{q,n} a_{-k+k'-q,n} a_{k,m} \}, \quad (8)$$

where the corresponding third- and fourth-order coefficients are

$$A_{n,m}^{(3)}(k) = -\frac{1}{4}S(g\mu_B)^2\sqrt{\frac{S}{2N'}}\left[\sum_{p=1}^N\{D_{n,p}^{yz}(0) + iD_{n,p}^{xy}(0)\}\delta_{n,m} + 4\{D_{n,m}^{yz}(k) + iD_{n,m}^{xy}(k)\}\right], \quad (9)$$

$$\begin{aligned} A_{n,m}^{(4)}(k) &= \frac{1}{4N'}\left\{J_{n,m}(k) + \frac{1}{2}(g\mu_B)^2D_{n,m}^{yy}(k)\right\}, \\ B_{n,m}^{(4)}(k) &= -\frac{1}{2N'}\left\{J_{n,m}(k) - (g\mu_B)^2D_{n,m}^{yy}(k)\right\}, \quad (10) \\ C_{n,m}^{(4)}(k) &= \frac{1}{8N'}(g\mu_B)^2\{D_{n,m}^{xx}(k) - D_{n,m}^{zz}(k) - 2iD_{n,m}^{xz}(k)\}. \end{aligned}$$

Here N' denotes the macroscopically large number of spins along the y axis of the stripe.

To study the interactions between SWs we need the results for the linear SWs, which were obtained already in our previous works.^{14,15} Here we outline the procedure briefly, so that a generalization can be made to higher-order processes. The linear SW term $H^{(2)}$ in Eq. (4) can be diagonalized by transforming from the a^\dagger and a operators to a new set of

boson operators b^\dagger and b , which satisfy the usual commutation relations and are defined by

$$a_{k,n} = \sum_{\ell=1}^N\{S_{n,\ell}(k)b_{k,\ell} + S_{n+N,\ell}^*(k)b_{-k,\ell}^\dagger\}. \quad (11)$$

Here $S_{n,\ell}(k)$ is an element of a $2N \times 2N$ transformation matrix \mathbf{S}_k calculated as in Refs. 15 and 14 and the creation operator $a_{k,n}^\dagger$ is expressed using the Hermitian conjugate of the above expression. The diagonalized form of $H^{(2)}$ becomes (apart from constant terms)

$$H^{(2)} = \sum_k \sum_{\ell=1}^N \omega_{k,\ell} b_{k,\ell}^\dagger b_{k,\ell}, \quad (12)$$

where the discrete SW frequencies are $\omega_{k,\ell}$.

The transformation in Eq. (11) can next be used to rewrite $H^{(3)}$ and $H^{(4)}$ in terms of the new operators that create or annihilate a SW of wave number k and branch label ℓ ($= 1, 2, \dots, N$), giving

$$\begin{aligned} H^{(3)} &= \sum_{\ell_1, \ell_2, \ell_3} \sum_{k, q} [V_1 b_{k, \ell_1}^\dagger b_{q, \ell_2}^\dagger b_{k+q, \ell_3} + V_2 b_{k, \ell_1}^\dagger b_{-q, \ell_2} b_{k+q, \ell_3} \\ &\quad + V_3 b_{k, \ell_1}^\dagger b_{q, \ell_2}^\dagger b_{-k-q, \ell_3}^\dagger + V_4 b_{-k, \ell_1} b_{-q, \ell_2} b_{k+q, \ell_3}], \quad (13) \end{aligned}$$

$$\begin{aligned} H^{(4)} &= \sum_{\ell_1, \ell_2, \ell_3, \ell_4} \sum_{k, k', q} [\Lambda_1 b_{k, \ell_1}^\dagger b_{k', \ell_2}^\dagger b_{q, \ell_3} b_{k+k'-q, \ell_4} + \Lambda_2 b_{k, \ell_1}^\dagger b_{-k', \ell_2} b_{q, \ell_3} b_{k+k'-q, \ell_4} + \Lambda_3 b_{k, \ell_1}^\dagger b_{k', \ell_2}^\dagger b_{-q, \ell_3}^\dagger b_{k+k'-q, \ell_4} \\ &\quad + \Lambda_4 b_{k, \ell_1}^\dagger b_{k', \ell_2}^\dagger b_{-q, \ell_3}^\dagger b_{-k-k'+q, \ell_4} + \Lambda_5 b_{-k, \ell_1} b_{-k', \ell_2} b_{q, \ell_3} b_{k+k'-q, \ell_4}]. \quad (14) \end{aligned}$$

The above summations over ℓ_i are over all N SW branches and the wave numbers are summed over the first Brillouin zone in one dimension. We note that each term in Eqs. (13) and (14) conserves the wave number, as expected from the translational symmetry in the y direction, but the SW branch labels can appear in all combinations. The amplitude factors $V_i(k, q | \ell_1, \ell_2, \ell_3)$ and $\Lambda_i(k, k', q | \ell_1, \ell_2, \ell_3, \ell_4)$ appearing in the above equations are lengthy expressions but they can be straightforwardly written down using Eqs. (7)–(11).

At this stage it is convenient to introduce a diagrammatic perturbation technique to study how the $H^{(3)}$ and $H^{(4)}$ terms modify the SW frequencies $\omega_{k,\ell}$ and introduce damping effects. This can be achieved following analogous calculations by Costa Filho *et al.*²⁰ for ultrathin ferromagnetic films. The formalism is similar because the atomic layer index used in Ref. 20 plays an analogous role to our label n as used in Eq. (4) to specify the spin sites in any cross section of the nanowire, while the two-dimensional in-plane wave vector for a film is replaced by our wave number k . Briefly, we define an $N \times N$ matrix causal Green's function $\mathbf{G}(k, i\omega_m)$ whose (ℓ, ℓ') element is just $\langle\langle b_{k,\ell}; b_{k,\ell'}^\dagger \rangle\rangle_{i\omega_m}$ in a standard notation where $\{i\omega_m\}$ is a set of imaginary boson frequencies.²¹ When evaluated with respect to $H^{(2)}$ in Eq. (12) as the unperturbed Hamiltonian, it is found that $\mathbf{G}(k, i\omega_m)$ is a diagonal matrix with its

elements proportional to $\delta_{\ell,\ell'}/(i\omega_m - \omega_{k,\ell})$. In a diagrammatic representation the noninteracting Green's function will be drawn as a solid directed line that can be labeled with $\{k, \ell, i\omega_m\}$, while the transformed $H^{(3)}$ and $H^{(4)}$ terms in Eqs. (13)–(14) define interaction vertices as represented in Fig. 2 with either three or four lines leaving (for a b^\dagger operator) or entering (for a b operator).

Then, following Ref. 20 for the film geometry, the modified poles of the matrix \mathbf{G} are found by introducing proper self-energy diagrams made up from the above interaction

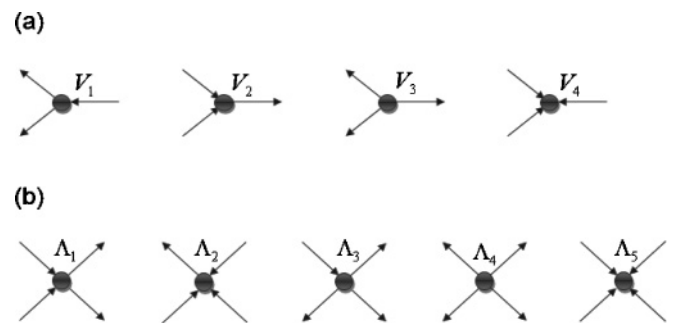


FIG. 2. Interaction vertices for (a) three-magnon processes and (b) four-magnon processes, showing the associated V_i and Λ_i factors.

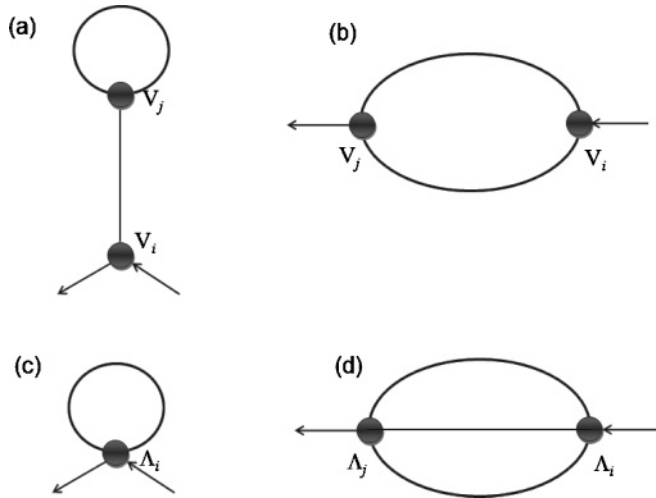


FIG. 3. Self-energy diagrams involving (a),(b) three-magnon processes and (c),(d) four-magnon processes. All possible combinations for the directions of arrows for the unlabeled Green's function lines must be considered.

vertices and lines. The relevant leading-order diagrams are those having the forms represented in Fig. 3. They have one external line $\{k, \ell, i\omega_m\}$ entering and another line $\{k, \ell, i\omega_m\}$ leaving, while the other lines and vertices are fully connected. The real and imaginary parts of these diagrams lead directly to formal expressions for the frequency shift $\Delta\omega_{k,\ell}$ and damping $\Gamma_{k,\ell}$, respectively, of the SW with wave number k and branch label ℓ [see Eq. (31) of Ref. 20]. Our results are described below with an interpretation of the diagrammatic representations.

We first consider the three-magnon processes. There are no diagrammatic self-energy terms that involve just one interaction vertex, since these vertices come in conjugate pairs (e.g., a V_1 with a V_2 or a V_3 with a V_4). This leads to diagrams with the topologies shown in Figs. 3(a) and 3(b). The first of these diagrams has a real value and so contributes only to the SW frequency shift, but the second diagram has a complex value and contributes to both the frequency shift and damping. Introducing the shorthand that $n_{k,\ell} = [\exp(\hbar\omega_{k,\ell}/k_B T) - 1]^{-1}$ denotes the Bose-Einstein thermal factor at temperature T for the linear SW with frequency $\omega_{k,\ell}$, the expressions for the SW frequency shift and damping due to three-magnon processes are eventually found to be

$$\begin{aligned} \Delta\omega_{k,\ell}^{(3)} &= - \sum_{\ell_1, \ell_2} \sum_q \left\{ \Psi_1 \frac{n_{q,\ell_1}}{\omega_{0,\ell_2}} + \Psi_2 \frac{n_{q,\ell_1} + n_{-k-q,\ell_2} + 1}{\omega_{-k-q,\ell_2} + \omega_{q,\ell_1} + \omega_{k,\ell}} \right. \\ &\quad \left. + \Psi_3 \frac{n_{q,\ell_1} - n_{k+q,\ell_2}}{\omega_{k+q,\ell_2} - \omega_{q,\ell_1} - \omega_{k,\ell}} + \Psi_4 \frac{n_{q,\ell_1} + n_{k-q,\ell_2} + 1}{\omega_{k-q,\ell_2} + \omega_{q,\ell_1} - \omega_{k,\ell}} \right\}, \end{aligned} \quad (15)$$

$$\begin{aligned} \Gamma_{k,\ell}^{(3)} &= -\pi \sum_{\ell_1, \ell_2} \sum_q \left\{ \Psi_3 [n_{q,\ell_1} - n_{k+q,\ell_2}] \right. \\ &\quad \times \delta(\omega_{k+q,\ell_2} - \omega_{q,\ell_1} - \omega_{k,\ell}) + \Psi_4 [n_{q,\ell_1} + n_{k-q,\ell_2} + 1] \\ &\quad \left. \times \delta(\omega_{k-q,\ell_2} + \omega_{q,\ell_1} - \omega_{k,\ell}) \right\}, \end{aligned} \quad (16)$$

where the weighting factors Ψ_i (with $i = 1, \dots, 4$), which are quadratic in the interaction vertices, are defined in Appendix A.

Also it is implicit that the principal value is taken in the summations in Eq. (15) where there are denominators that could vanish. The two δ -function terms in Eq. (16), which conserve energy and longitudinal wave number, correspond to three-magnon confluence and splitting processes, respectively. We note that the SW processes involve either the same branch or different branches.

Now we turn to the four-magnon processes. In this case there is a nonvanishing diagram that has one interaction vertex, as depicted in Fig. 3(c). It is real and upon evaluation gives the following contribution to the SW frequency shift:

$$\Delta\omega_{k,\ell}^{(4)} = \sum_{\ell_1} \sum_q \Phi_1 n_{q,\ell_1}, \quad (17)$$

where the weighting factor Φ_1 is defined in Appendix A as a linear combination of Λ_1 vertices. To obtain the leading-order result for the SW damping due to four-magnon processes it is necessary to consider diagrams with two vertices having the topologies represented in Fig. 3(d). The result takes the general form

$$\begin{aligned} \Gamma_{k,\ell}^{(4)} &= -\pi \sum_{\ell_1, \ell_2, \ell_3} \sum_{q, q'} \left\{ \Phi_2 n_2^{\text{th}}(T) \delta(\omega_{q,\ell_1} - \omega_{q',\ell_2} - \omega_{k+q-q',\ell_3} \right. \\ &\quad \left. + \omega_{k,\ell}) + \Phi_3 n_3^{\text{th}}(T) \delta(-\omega_{q,\ell_1} - \omega_{q',\ell_2} - \omega_{k-q-q',\ell_3} \right. \\ &\quad \left. + \omega_{k,\ell}) + \Phi_4 n_4^{\text{th}}(T) \delta(\omega_{q,\ell_1} - \omega_{q',\ell_2} - \omega_{-k+q-q',\ell_3} - \omega_{k,\ell}) \right\}. \end{aligned} \quad (18)$$

Here $n_2^{\text{th}}(T)$ and $n_3^{\text{th}}(T)$ represent combinations of thermal factors defined by

$$\begin{aligned} n_2^{\text{th}}(T) &= n_{q,\ell_1} [n_{q',\ell_2} + n_{k+q-q',\ell_3} + 1] - n_{q',\ell_2} n_{k+q-q',\ell_3}, \\ n_3^{\text{th}}(T) &= [n_{q,\ell_1} + 1] [n_{q',\ell_2} + n_{k-q-q',\ell_3} + 1] + n_{q',\ell_2} n_{k-q-q',\ell_3}, \end{aligned} \quad (19)$$

while $n_4^{\text{th}}(T)$ is obtained from $n_2^{\text{th}}(T)$ by everywhere replacing k by $-k$. The weighting factors $\Phi_{2,3,4}$ are discussed in Appendix A. There are now three types of δ -function terms, of which the first (proportional to Φ_2) corresponds to four-magnon scattering and the next two are generalized four-magnon splitting and confluence processes. Again there can be intrabranch and interbranch contributions.

The combined SW frequency shift is $\Delta\omega_{k,\ell} = \Delta\omega_{k,\ell}^{(3)} + \Delta\omega_{k,\ell}^{(4)}$ and the combined damping is $\Gamma_{k,\ell} = \Gamma_{k,\ell}^{(3)} + \Gamma_{k,\ell}^{(4)}$. The relative importance of the three- and four-magnon processes in these expressions will depend on factors such as the relative strengths of the dipole-dipole and exchange interactions, the wave number k , the external field H_0 , and the temperature T . It may also depend on the branch label ℓ of the SW.

B. Transverse applied field

It is a more challenging problem to calculate the nonlinear magnetization dynamics in the case of an external field of arbitrary magnitude H_0 applied *perpendicular* to the stripe, i.e., taken along the z axis in Fig. 1. The spins are now canted away from the symmetry (y) axis, resulting in strong spatial inhomogeneities of the magnetization. Eventually, for large enough H_0 the equilibrium magnetization lies approximately

along the z direction, but with some inhomogeneities still remaining at the lateral edges. Discussion of the linear SW spectrum for this situation was included in our previous work.^{14,15} We now extend this treatment to the nonlinear case, for which we eventually conclude that the SW damping can be much larger (depending on the magnitude of the transverse H_0) than found in the preceding subsection for a longitudinal applied field.

Before proceeding to the SW properties we deduce the equilibrium configuration of the spins by following the approach described in Ref. 14 for cylindrical nanowires. We denote the equilibrium value of any spin vector \mathbf{S}_{in} by $\tilde{\mathbf{S}}_n$, which will be independent of i due to translational symmetry. Here n (with $n = 1, \dots, N$, as before) labels the spin sites in any cross section of the wire and i labels the coordinate along the length of the wire. Briefly, a starting configuration of spins $\{\mathbf{S}_{i,n}\}$ is assumed, and then the total effective field at each spin site is calculated using $\mathbf{H}_{i,n}^{\text{eff}} = -(1/g\mu_B)(\delta E/\delta \mathbf{S}_{i,n})$, where E is the energy functional deduced from the Hamiltonian in Eq. (1). Next we align each spin parallel to the total effective field at that site to obtain a new spin configuration. The above process is repeated until there is convergence, i.e., all the products $|\mathbf{S}_n \times \mathbf{H}_n^{\text{eff}}|$ are negligible, implying that the torques acting on the spins vanish. This procedure is repeated with different initial configurations and a set of local minima is obtained. The global equilibrium configuration at $T \ll T_C$ is adopted as being the one with the smallest energy E .

We now specify the equilibrium configuration $\{\tilde{\mathbf{S}}_n\}$ in terms of two sets of angles $\{\alpha_n, \theta_n\}$ in polar coordinates, which depend on position in the cross section when the magnetization is inhomogeneous. Thus we have $\tilde{\mathbf{S}}_n = (\tilde{S}_n^z, \tilde{S}_n^x, \tilde{S}_n^y) = S(\sin \alpha_n \cos \theta_n, \sin \alpha_n \sin \theta_n, \cos \alpha_n)$. When introducing the spin dynamics it is convenient to define a local coordinate system (z', x', y') for each spin \mathbf{S}_n such that the y' axis is directed along the equilibrium orientation of that spin, as in Ref. 14. The relationships between the spin components in the global (z, x, y) and local (z', x', y') coordinates are

$$\begin{aligned} S_{i,n}^z &= \cos \alpha_n \cos \theta_n S_{i,n}^{z'} - \sin \theta_n S_{i,n}^{x'} + \sin \alpha_n \cos \theta_n S_{i,n}^{y'} \\ S_{i,n}^x &= \cos \alpha_n \sin \theta_n S_{i,n}^{z'} + \cos \theta_n S_{i,n}^{x'} + \sin \alpha_n \sin \theta_n S_{i,n}^{y'} \\ S_{i,n}^y &= -\sin \alpha_n S_{i,n}^{z'} + \cos \alpha_n S_{i,n}^{y'} \end{aligned} \quad (20)$$

As in the previous subsection, the Holstein-Primakoff transformation can again be utilized, except that now it is applied in the *local* coordinate system to rewrite $S_{in}^{y'}$ and $S_{in}^{\pm} = S_{in}^{z'} \pm i S_{in}^{x'}$ in terms of boson creation and annihilation operators. The transformation is substituted into the spin Hamiltonian which is expanded in term of the boson operators as was done in Eq. (3) for the longitudinal case at low temperatures $T \ll T_C$.

The first-order term $H^{(1)}$ again vanishes, when the constant term $H^{(0)}$ is minimized and the local axes are chosen as described above. The higher-order terms $H^{(2)}$, $H^{(3)}$, and $H^{(4)}$ have the same interpretations as previously and can be represented in the same general forms as in Eqs. (4), (7), and (8). The only difference is that the coefficients $A_{n,m}^{(2)}(k)$, $B_{n,m}^{(2)}(k)$, $A_{n,m}^{(3)}(k)$, $A_{n,m}^{(4)}(k)$, $B_{n,m}^{(4)}(k)$, and $C_{n,m}^{(4)}(k)$ must all be redefined because of their dependence on the canting angles

α_n and θ_n for the transverse field case. The modified forms of these coefficients are quoted in Appendix B.

It then follows that, with the above redefinitions, the main results that were derived for the SW properties in the previous subsection still apply. In particular, the same formalism holds for the $2N \times 2N$ transformation matrix \mathbf{S}_k in Eq. (11) leading to Eq. (12) for the diagonalized $H^{(2)}$ giving the noninteracting SW frequencies $\omega_{k,\ell}$. Moreover, the previous formal expressions derived for the SW frequency shift and damping in Eqs. (15)–(18) also apply in the transverse field case.

III. NUMERICAL RESULTS FOR THE LONGITUDINAL CASE

Numerical calculations based on the above theory are presented first for the simpler case of a longitudinal applied field. The material parameters used in our approach are the exchange stiffness $D = SJa^2/g\mu_B$, the saturation magnetization $M_s = g\mu_B S/a^3$, and the gyromagnetic ratio $\gamma/2\pi = g\mu_B$. We will make comparisons with FMR data for the SW damping in Permalloy stripes.¹¹ Measurements by those authors gave $M_s = 0.058$ T and $g\mu_B = 29.5$ GHz/T for their samples, and we take $D = 24$ T nm² for Permalloy as in Ref. 22. Our SW frequency shift and damping results will be obtained for the smallest of the experimental stripe samples, which corresponded to width $W = 125$ nm and thickness $L = 6$ nm. The experiments¹¹ were done at room temperature which is well below $T_C \sim 850$ K for the Curie temperature of Permalloy, so the approximations of our boson expansion technique should still be appropriate. In order to establish a temperature scale in the theory, we estimate T_C from mean-field theory for a site at the center of the stripe (including the static dipole-dipole field, as well as the static exchange field) and we set this equal to the experimental value. This enables us to present our theoretical estimates for a range of T/T_C values from 0 up to about 0.35. The summations over the internal wave numbers in Eqs. (15)–(18) were carried out numerically by dividing the one-dimensional Brillouin zone (from $-\pi/a$ to π/a , where a is the effective lattice parameter discussed earlier) into typically 2000 intervals, which we tested gave good convergence. Also we chose $a = 3$ nm, which is smaller than the exchange length $a_{Ex} \simeq 5.3$ nm of Permalloy, and a longitudinal applied field of 0.06 T, which is within the range used in the experiments.¹¹

First, for comparison, we show in Fig. 4 the calculated low-temperature dispersion relations for the linear SW in the Permalloy stripe. The quantized SW branches show the expected behavior (with an upward slope due to exchange effects over most of the range of k) for a stripe of relatively small cross section. By contrast, for stripes with larger cross sections, it would be evident that the lowest few branches show an initial dip in frequency at very small k due to the dipole-dipole effects (e.g., see Fig. 2 in Ref. 15).

Next, in Fig. 5 some calculations are presented for the three-magnon damping in the same Permalloy stripe plotted against wave number k for the SW branch with $\ell = 2$ (the second lowest in Fig. 4). The contributions from the confluence and the splitting processes are shown separately, as well as the total damping. Here the confluence processes dominate and

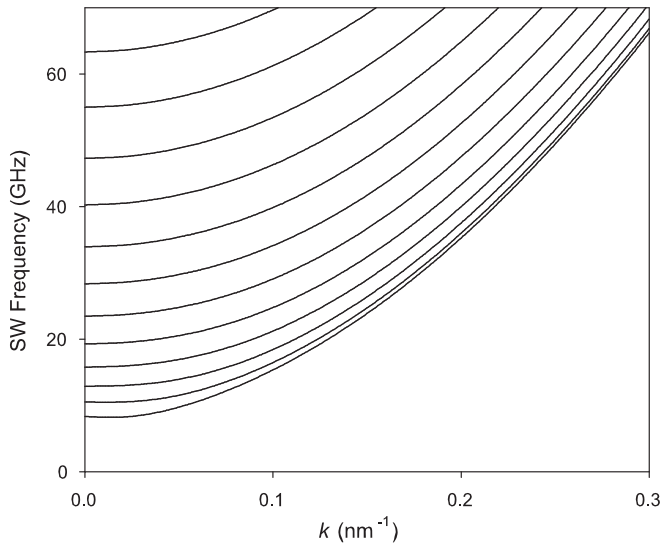


FIG. 4. Linear SW frequencies vs wave number k for a Permalloy stripe with cross section $6 \text{ nm} \times 125 \text{ nm}$ and longitudinal field $\mu_0 H_0 = 0.06 \text{ T}$. The physical parameters are given in the text. Only the lowest SW modes are shown.

they can occur for all k , whereas there is a “threshold” value for splitting processes (at $k \sim 0.11 \text{ nm}^{-1}$ in this example) below which it is not possible energetically for a SW with the specified $\{k, \ell\}$ to decay into two other SW on the same or any other branches. This can be understood by reference to Fig. 4. The threshold values become smaller for higher SW branches (larger ℓ), and eventually disappear, because there are decay channels involving the lower branches. All possible interbranch, as well as intrabranh, effects have been taken into account here in calculating the damping. These results

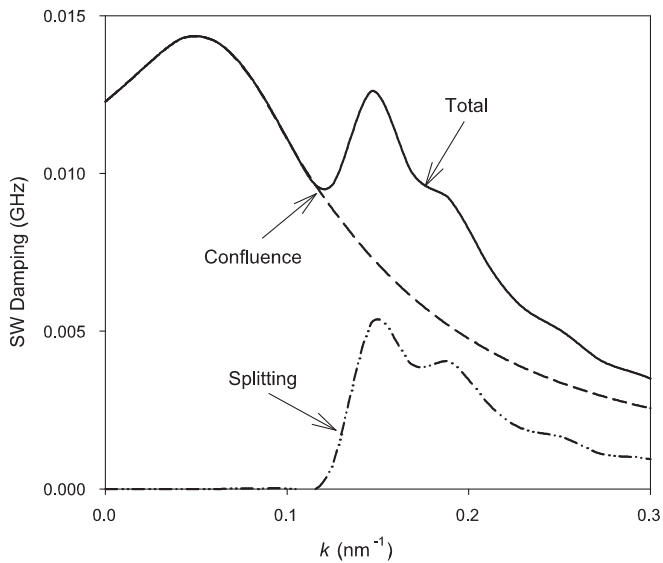


FIG. 5. Three-magnon damping of the SW branch with $\ell = 2$ vs wave number k for a Permalloy stripe with cross section $6 \text{ nm} \times 125 \text{ nm}$, $T/T_C = 0.3$, and longitudinal field $\mu_0 H_0 = 0.06 \text{ T}$. The different lines show the total damping, as well as the confluence and splitting processes, as labeled.

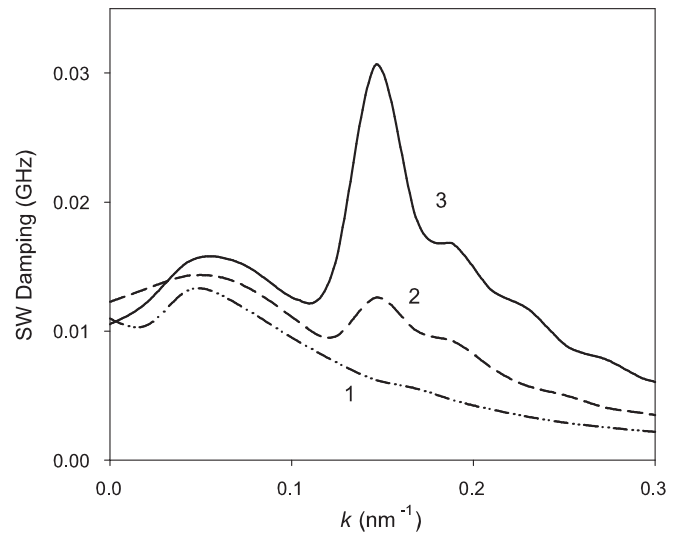


FIG. 6. Total three-magnon damping of the three lowest SW branches ($\ell = 1, 2, 3$) vs wave number k for the same Permalloy stripe as in Fig. 4 in a longitudinal field. The three lines correspond to the SW branches as labeled.

were obtained using Eq. (16) for $\Gamma_{k,\ell}^{(3)}$, which we estimate to be much larger than the four-magnon damping in this case.

In Fig. 6 we compare the k dependence of the total (confluence plus splitting) three-magnon damping for the lowest three SW branches. The results are broadly similar for the different branches, but they display an overall trend for the damping to increase with increasing branch label ℓ . This behavior is particularly evident for $k \sim 0.15 \text{ nm}^{-1}$, where it is mainly due to an increase in contributions from the three-magnon splitting terms. Another comparison, with respect to the temperature dependence of the damping, is given in Fig. 7. Here the calculations are for the lowest SW branch ($\ell = 1$) and show the total three-magnon damping at a

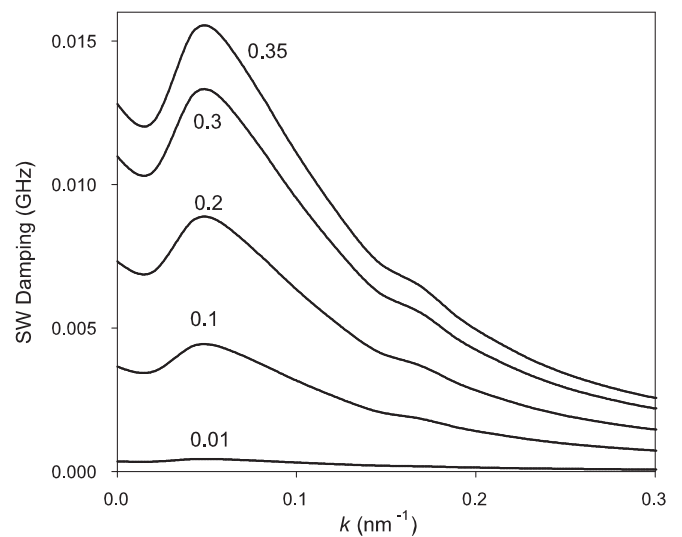


FIG. 7. Three-magnon damping at different temperatures for the lowest SW branch ($\ell = 1$) vs wave number k for the same Permalloy stripe as in Fig. 4 in a longitudinal field. The lines correspond to different T/T_C values as labeled.

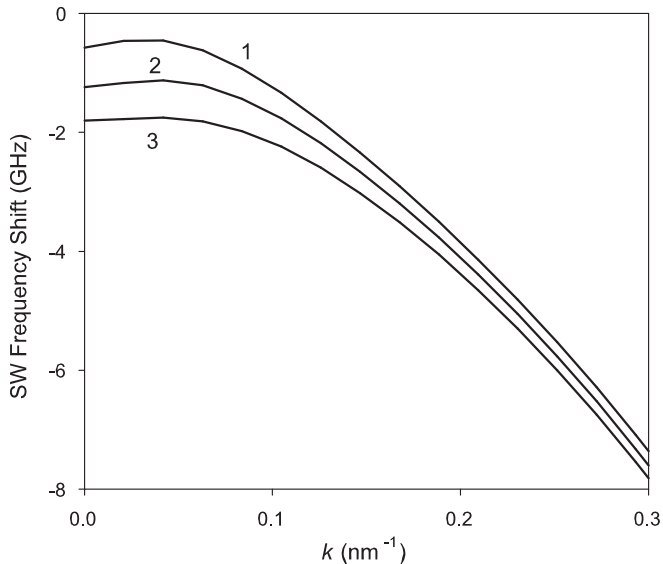


FIG. 8. Four-magnon frequency shift of the three lowest SW branches ($\ell = 1, 2, 3$) vs wave number k for the same Permalloy stripe as in Fig. 4 in a longitudinal field. The three lines correspond to the SW branches as labeled.

series of T/T_C values up to 0.35. At each k value it is seen that there is a monotonic increase in the damping with temperature, which is mainly due to an increase in the Bose-Einstein thermal factors appearing in Eq. (16).

Finally in this section we show in Fig. 8 some calculations for the SW frequency shift arising due to the SW interactions. By contrast to the damping results, it is found in this case that the dominant contribution for Permalloy at almost all values of k and T/T_C come from the four-magnon processes as given by Eq. (17). This is mainly because the four-magnon frequency shift has a leading-order contribution that is *linear* in the interaction vertex, as was discussed in the context of Fig. 3(c), whereas the contribution calculated from Eq. (15) is quadratic in the three-magnon interaction vertices and is smaller in magnitude. The results in Fig. 8 show that the four-magnon frequency shift is negative and increases in magnitude with k , which are characteristics of the behavior for Heisenberg ferromagnets.¹⁶ However, at very small k (below $\sim 0.04 \text{ nm}^{-1}$) in Fig. 8 there is a region where the frequency shift decreases in magnitude, and this is attributable to the dipole-dipole interactions. Figure 8 also shows that $|\Delta\omega_{k,\ell}|$ tends to increase with branch label ℓ .

The results presented here for the dominant three-magnon damping are discussed further in relation to the Boone *et al.*¹¹ experimental studies in Sec. V.

IV. NUMERICAL RESULTS FOR THE TRANSVERSE CASE

Next we consider numerical results for the case when the magnetic field is applied perpendicular to the stripe axis (along the z axis). Although the recent SW damping measurements¹¹ applied only for a longitudinal field, the transverse case is more interesting because both the static and the dynamic magnetization throughout the sample may be strongly inhomogeneous, and we will show here that the damping effects in particular can become much larger.

Before considering a stripe with finite thickness and width it is instructive to consider briefly what happens for an ultrathin wire, i.e., a wire consisting of a single line of dipole-exchange coupled spins, when placed in a transverse field. This is just the special case of $N = 1$ in our theory, so all the spins along the line are canted in the yz plane at the same angle θ from the y axis. It is easy to show that the equilibrium configuration for the spins (see Sec. II A) corresponds simply to

$$\sin \theta = H_0/H_c \quad (H_0 \leq H_c), \quad (21)$$

while $\theta = 90^\circ$ if $H_0 > H_c$, where H_c is a characteristic field related to a static dipole-dipole sum by $H_c = -(3/2)Sg\mu_B D^{yy}(0) > 0$ in the notation of Sec. I. At $k = 0$ the frequency of the single SW branch (for the noninteracting case) can be shown to decrease as H_0 is increased from zero until it vanishes when $H_0 = H_c$, i.e., the $k = 0$ SW exhibits a soft-mode behavior. For $H_0 > H_c$ the SW frequency increases with H_0 . Also there is a simplification for the three-magnon interaction terms V_i , which are all proportional to $\sin(2\theta)$, therefore implying that the three-magnon damping has an

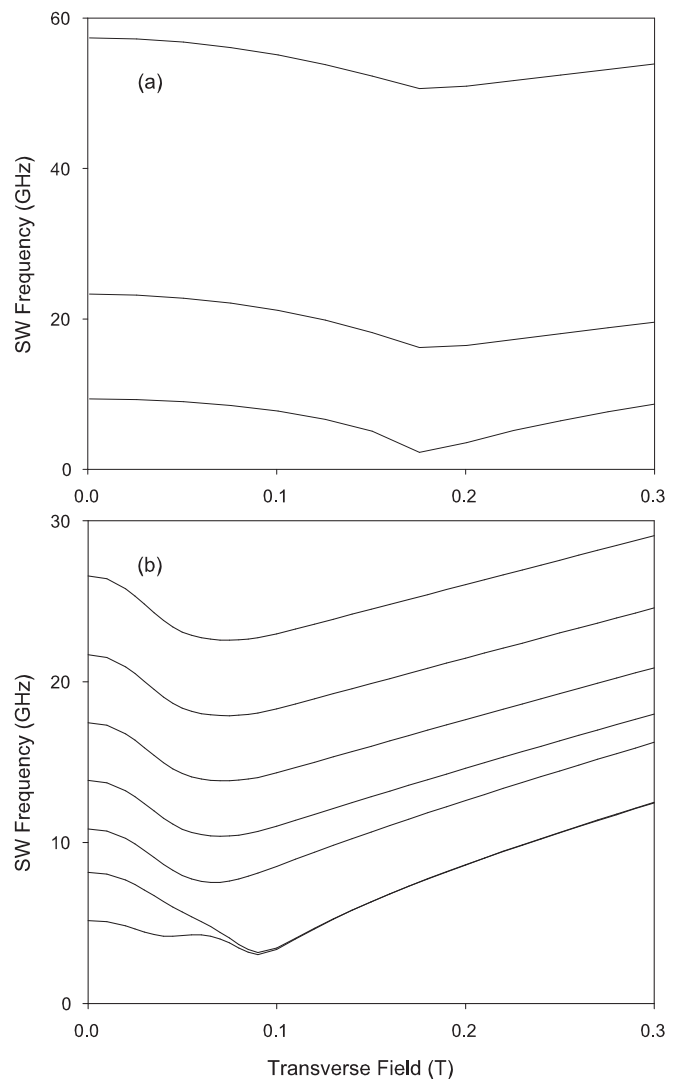


FIG. 9. Linear SW frequencies at $k = 0$ vs transverse magnetic field H_0 for a Permalloy stripe with cross section (a) $6 \text{ nm} \times 24 \text{ nm}$ and (b) $6 \text{ nm} \times 125 \text{ nm}$. Only the few lowest SW modes are shown.

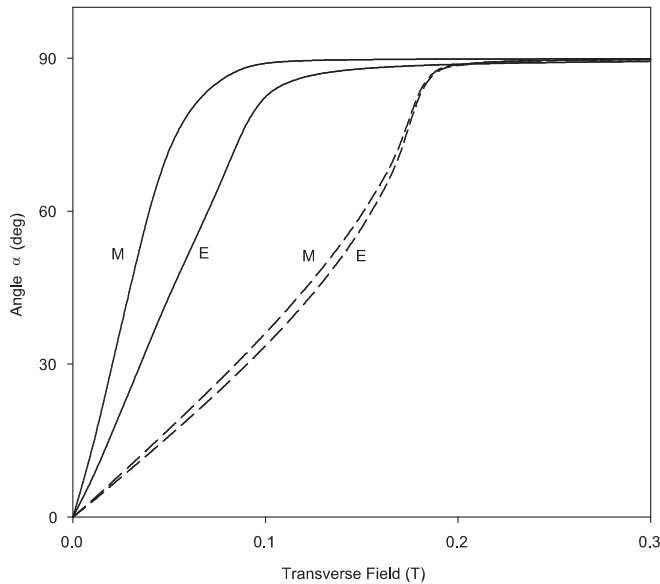


FIG. 10. Polar angle α vs transverse magnetic field H_0 for Permalloy stripes with cross sections $6 \text{ nm} \times 24 \text{ nm}$ (dashed curves) and $6 \text{ nm} \times 125 \text{ nm}$ (solid curves). Labels M and E refer to the middle and lateral edges of the stripes, respectively.

overall proportionality to $\sin^2(2\theta)$ for a single line. This has its largest value when $\theta \sim 45^\circ$ or $H_0 \sim 0.7H_c$. While this simple dependence does not hold for a wire stripe of finite width and thickness, it does strongly suggest that the transverse field case will be of interest for the field dependence, and it may lead to a larger three-magnon damping than was found for the case of a stripe in a longitudinal field. The three-magnon damping is not zero for a stripe in a longitudinal field (by contrast with the single line of spins with $\theta = 0$) because of the position dependence of the dipole-dipole sums and the interbranch SW effects.

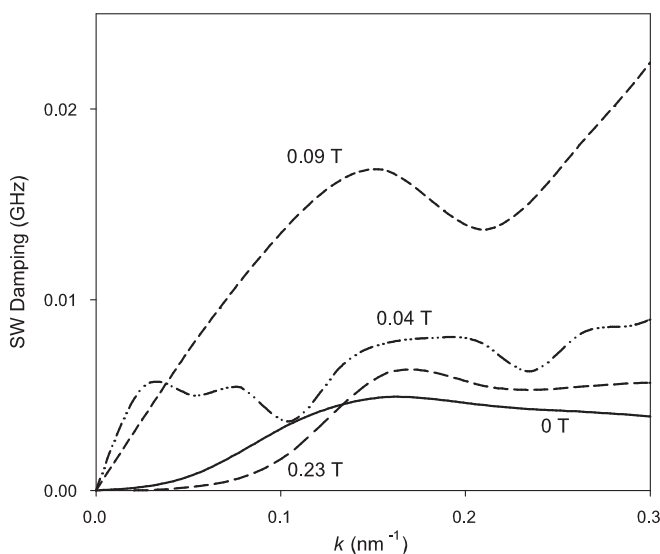


FIG. 11. Three-magnon damping of the lowest SW branch ($\ell = 1$) vs wave number k for a Permalloy stripe with cross section $6 \text{ nm} \times 24 \text{ nm}$, $T/T_C = 0.3$, and different values of transverse magnetic field H_0 as indicated.

In the following numerical applications we shall consider two different stripe sizes to illustrate the different types of behavior. We again use Permalloy for the examples, with material parameters chosen as in the previous section, but we take two values for the width-to-thickness aspect ratio W/L . The smaller stripe is chosen to have $W = 24 \text{ nm}$ and $L = 6 \text{ nm}$, while the larger stripe has the same dimensions as previously, i.e., $W = 125 \text{ nm}$ and $L = 6 \text{ nm}$. In Fig. 9 the calculated linear SW frequencies at $k = 0$ are plotted versus the applied field for the two structures. The reduced width of the stripe in Fig. 9(a) causes the frequencies of the quantized SW modes to be further apart, and we see that the lowest branches have a minimum when the transverse field $\sim 0.18 \text{ T}$. This is analogous to the characteristic field H_c mentioned for the single line of spins. It is the field value above which all of the spins in any cross section have their equilibrium orientations roughly in the transverse (z) direction. The frequency of the lowest mode does not actually dip to zero because there is not a precise reorientation. There is a contrasting behavior for the wider stripe in Fig. 9(b), where the SW modes are closer together, as expected. It is also seen that the lowest two modes become degenerate as H_0 is increased and they have a pronounced minimum at a field value of $\sim 0.09 \text{ T}$, whereas the higher branches ($\ell \geq 3$) show dips at $\sim 0.06 \text{ T}$. Actually the lowest curve also has a shallow minimum at $\sim 0.055 \text{ T}$. As explained in our previous paper on the linear SW in stripes,¹⁵ “edge modes” can form as regions of strong spatial inhomogeneities in the magnetization at the two lateral edges when W/L is sufficiently large. In effect, there are two characteristic fields for this case, one at $\sim 0.06 \text{ T}$ associated with the reorientation of the spins in the interior of the stripe and another at $\sim 0.09 \text{ T}$ associated with the reorientation of the spins in the edge regions. This type of behavior for the SW modes can be seen in Brillouin light scattering data (e.g., see Fig. 3 of Ref. 23). The above conclusions regarding the inhomogeneous magnetization and the characteristic fields are reinforced by Fig. 10, where the mean polar angle α is plotted versus the transverse applied field for sites in the middle and

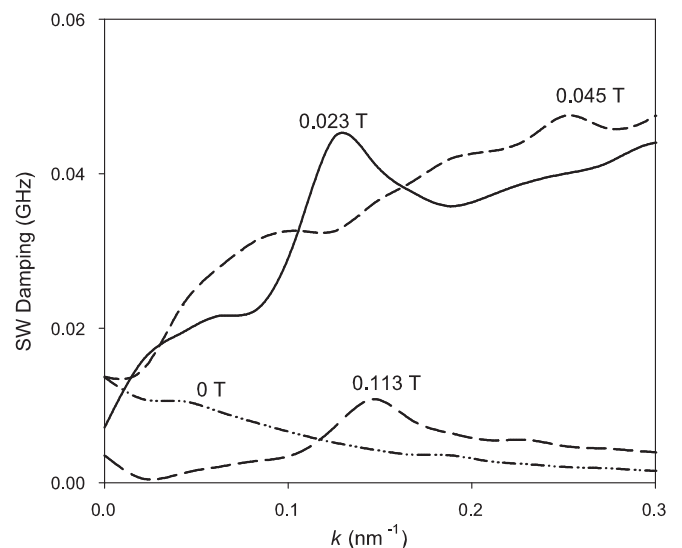


FIG. 12. Same as in Fig. 11 but for the larger stripe with cross section $6 \text{ nm} \times 125 \text{ nm}$.

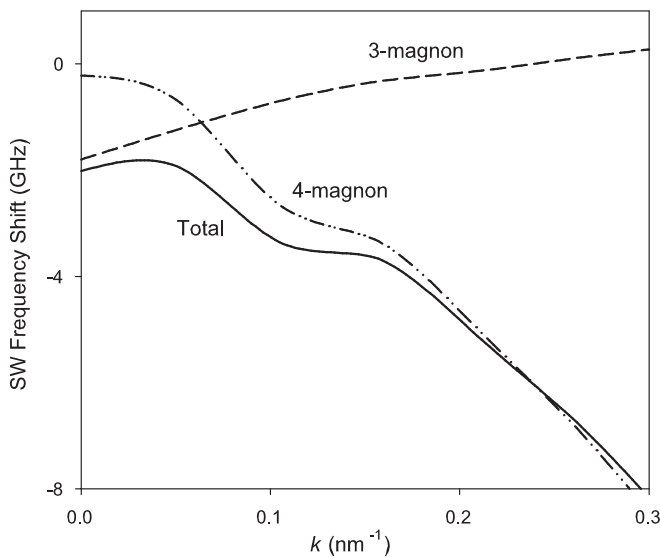


FIG. 13. The frequency shift of the lowest ($\ell = 1$) SW branch vs wave number k for a Permalloy stripe with cross section $6 \text{ nm} \times 24 \text{ nm}$, $T/T_C = 0.3$, and transverse field $\mu_0 H_0 = 0.14 \text{ T}$. The different lines show the total, three-magnon, and four-magnon frequency shifts, as labeled.

the lateral edges of each stripe. We recall that the local magnetization component along the stripe axis is proportional to $\cos \alpha$.

It is again the case that the three-magnon damping in these samples is dominant over the four-magnon damping, and we show numerical examples in Figs. 11 and 12 for the two stripes where $\Gamma_{k,\ell}^{(3)}$ is plotted against wave number k for several different transverse field values. It can be seen from Fig. 11 for the narrower stripe that the damping is relatively small when the transverse field is either zero or 0.23 T (which is above the characteristic value of $\sim 0.18 \text{ T}$ for this stripe). These cases correspond, respectively, to the equilibrium orientation of the spins being aligned longitudinally or mainly transverse. By contrast, for the intermediate field values of 0.04 T and particularly 0.09 T, the spins are strongly canted and the damping is generally larger. Similar data are presented in Fig. 12 for the wider stripe with similar conclusions for the damping at different transverse fields relative to the characteristic field values of that stripe.

Finally, in Fig. 13 we show some calculations for the SW frequency shift $\Delta\omega_{k,\ell}$ versus k in a transverse field, taking the smaller stripe size and the lowest ($\ell = 1$) branch. The behavior is broadly similar to that for the longitudinal field case (see Fig. 8) where the four-magnon contribution was dominant, except that in the transverse field case it can be seen that there are significant corrections at smaller k (less than $\sim 0.1 \text{ nm}^{-1}$) due to three-magnon processes. The chosen transverse field value of 0.14 T is about 0.8 of the characteristic field value for reorientation of the spins along the z axis; so the spins are canted, making the three-magnon effects more significant in this case.

V. DISCUSSION AND CONCLUSIONS

In this paper we have used a Hamiltonian-based approach to derive the explicit expressions for the terms $H^{(3)}$ and $H^{(4)}$ that

describe the three- and four-magnon processes, respectively, in a ferromagnetic stripe geometry, taking the external field to be applied either in the longitudinal (y) direction or the transverse (z) direction. The allowed processes conserve the longitudinal wave number k , since this is associated with the direction of translational symmetry, but there is a mixing of all the different SW branch labels ℓ that are involved. These nonlinear terms were then employed to obtain expressions for the frequency shift and damping of any SW characterized by $\{k,\ell\}$ as a function of temperature T and applied field H_0 .

Numerical calculations were made for stripes of Permalloy, taking the width and thickness the same as for the FMR experimental studies in Ref. 11. In the case of a longitudinal applied field, as in the experiments, it was found that the three-magnon confluence and splitting contributions to the damping dominated over the four-magnon contributions. However, at $k \approx 0$ (as in the FMR experiments) the splitting processes are suppressed for the lower branches because there are threshold wave numbers that must be exceeded, so the three-magnon confluence terms dominate for the lowest three SW branches, as concluded in Ref. 11. On the other hand, for the SW frequency shift we concluded that the four-magnon scattering term (which contributed in first order) was dominant. Quantitative comparison with Boone *et al.*¹¹ is made difficult by the fact that their damping results include other contributions presumed to be two-magnon effects. These occur when a SW with a given k decays into another SW with the same frequency, but on a different branch (and with a different wave number). It occurs if disorder in the sample destroys the translational symmetry along the stripe, and it was suggested in Ref. 11 that roughness at the lateral edges of the stripes might be responsible. Such contributions do not arise in our calculation because translational symmetry is assumed and roughness effects are not modeled. Other aspects of the behavior for the three-magnon confluence damping are found to be broadly consistent with Ref. 11. For example, the calculated damping tends to increase with increasing branch label ℓ (because there are more decay channels available) and we found that it also tends to increase if H_0 is reduced in magnitude (mainly because the linear SW frequencies are reduced, thus increasing the Bose-Einstein thermal factors at a given temperature). We noticed a dependence on the stripe width W , whereby the damping tends to be larger for larger W (in part, due to the formation of edge modes).

It was shown that our calculations could straightforwardly be extended to the case of a transverse field. Here the numerical calculations indicated that the damping could be significantly larger than in the longitudinal field case, so it would be interesting to have experimental data for this situation. The enhanced damping is predicted to occur when the magnitude of H_0 is less than the characteristic field for reorientation of the magnetization to the transverse direction, and we presented estimates for the same type of stripe sample as used for the longitudinal measurements.¹¹

Finally we remark that the results obtained here for the interaction vertices can be applied to study other nonlinear SW properties, such as SW instabilities in the presence of pumping fields (see e.g., Ref. 24) or SW behavior in magnonic crystals (see e.g., Refs. 8 and 25).

ACKNOWLEDGMENTS

We acknowledge support from the Natural Science and Engineering Research Council (NSERC) of Canada and the Shared Hierarchical Academic Research Computing Network (SHARCNet).

APPENDIX A: THREE- AND FOUR-MAGNON WEIGHTING FACTORS

The three-magnon weighting factors Ψ_i with $i = 1, \dots, 4$ that were introduced in Eqs. (15) and (16) are defined by

$$\begin{aligned}\Psi_1 &= \{V_1(0, q|\ell_2, \ell_1, \ell_1) + V_1(q, 0|\ell_1, \ell_2, \ell_1)\}\{V_2(k, -k|\ell, \ell, \ell_2) + V_2(k, 0|\ell, \ell_2, \ell)\} \\ &\quad + \{V_1(k, 0|\ell, \ell_2, \ell) + V_1(0, k|\ell_2, \ell, \ell)\}\{V_2(q, 0|\ell_1, \ell_2, \ell_1) + V_2(q, -q|\ell_1, \ell_1, \ell_2)\}, \\ \Psi_2 &= \frac{1}{2}\{V_3(k, q|\ell, \ell_1, \ell_2) + V_3(k, -k - q|\ell, \ell_2, \ell_1) + V_3(q, k|\ell_1, \ell, \ell_2) \\ &\quad + V_3(q, -k - q|\ell_1, \ell_2, \ell) + V_3(-k - q, k|\ell_2, \ell, \ell_1) + V_3(-k - q, q|\ell_2, \ell_1, \ell)\} \\ &\quad \times \{V_4(-k, -q|\ell, \ell_1, \ell_2) + V_4(-k, k + q|\ell, \ell_2, \ell_1) + V_4(-q, -k|\ell_1, \ell, \ell_2) \\ &\quad + V_4(-q, k + q|\ell_1, \ell_2, \ell) + V_4(k + q, -k|\ell_2, \ell, \ell_1) + V_4(k + q, -q|\ell_2, \ell_1, \ell)\}, \\ \Psi_3 &= \{V_1(k, q|\ell, \ell_1, \ell_2) + V_1(q, k|\ell_1, \ell, \ell_2)\}\{V_2(k + q, -k|\ell_2, \ell, \ell_1) + V_2(k + q, -q|\ell_2, \ell_1, \ell)\}, \\ \Psi_4 &= \frac{1}{2}\{V_1(q, k - q|\ell_1, \ell_2, \ell) + V_1(k - q, q|\ell_2, \ell_1, \ell)\}\{V_2(k, -q|\ell, \ell_1, \ell_2) + V_2(k, q - k|\ell, \ell_2, \ell_1)\}.\end{aligned}$$

The four-magnon weighting factor Φ_1 in Eq. (17) is defined by

$$\Phi_1 = \Lambda_1(k, q, k|\ell, \ell_1, \ell, \ell_1) + \Lambda_1(k, q, q|\ell, \ell_1, \ell_1, \ell) + \Lambda_1(q, k, k|\ell_1, \ell, \ell, \ell_1) + \Lambda_1(q, k, q|\ell_1, \ell, \ell_1, \ell), \quad (\text{A1})$$

while Φ_2 in Eq. (18) is

$$\begin{aligned}\Phi_2 &= \frac{1}{2}\{\Lambda_1(k, q, q'|\ell, \ell_1, \ell_2, \ell_3) + \Lambda_1(k, q, k + q - q'|\ell, \ell_1, \ell_3, \ell_2) + \Lambda_1(q, k, q'|\ell_1, \ell, \ell_2, \ell_3) \\ &\quad + \Lambda_1(q, k, k + q - q'|\ell_1, \ell, \ell_3, \ell_2)\}\{\Lambda_1(q', k + q - q', k|\ell_2, \ell_3, \ell, \ell_1) + \Lambda_1(q', k + q - q', q|\ell_2, \ell_3, \ell_1, \ell) \\ &\quad + \Lambda_1(k + q - q', q', k|\ell_3, \ell_2, \ell, \ell_1) + \Lambda_1(k + q - q', q', q|\ell_3, \ell_2, \ell_1, \ell)\}.\end{aligned} \quad (\text{A2})$$

There are similar expressions for Φ_3 and Φ_4 that can be written down as required.

APPENDIX B: HAMILTONIAN COEFFICIENTS IN THE TRANSVERSE CASE

When the applied field is in the transverse directions, the definitions of the coefficients $A_{n,m}^{(2)}$ and $B_{n,m}^{(2)}$ appearing in Eq. (4) are modified to

$$\begin{aligned}A_{n,m}^{(2)}(k) &= \left[-2S \sum_{p=1}^N \sum_{\alpha, \beta} \chi_{n,p}^{\alpha\beta}(0) Q_n^\alpha Q_p^\beta + g\mu_B H_0 Q_n^z \right] \delta_{nm} + \frac{S}{2} \sum_{\alpha, \beta} \chi_{n,m}^{\alpha\beta}(k) [P_n^\alpha (P_m^\beta)^* + P_n^\beta (P_m^\alpha)^*], \\ B_{n,m}^{(2)}(k) &= \frac{S}{2} \sum_{\alpha, \beta} \chi_{n,m}^{\alpha\beta}(k) P_n^\alpha P_m^\beta,\end{aligned} \quad (\text{B1})$$

where \mathbf{P}_n and \mathbf{Q}_n are defined in terms of the angles $\{\alpha_n, \theta_n\}$ and the unit vectors along the x , y , and z axes, while the $\chi_{n,m}^{\alpha\beta}(k)$ are dipole-exchange terms:

$$\begin{aligned}\mathbf{P}_n &= (\cos \alpha_n \sin \theta_n + i \cos \theta_n) \mathbf{x} - \sin \alpha_n \mathbf{y} \\ &\quad + (\cos \alpha_n \cos \theta_n - i \sin \theta_n) \mathbf{z}, \\ \mathbf{Q}_n &= \sin \alpha_n \sin \theta_n \mathbf{x} + \cos \alpha_n \mathbf{y} + \sin \alpha_n \cos \theta_n \mathbf{z},\end{aligned} \quad (\text{B2})$$

$$\chi_{n,m}^{\alpha\beta}(k) = \frac{1}{2} [(g\mu_B)^2 D_{n,m}^{\alpha\beta}(k) - J_{n,m}(k) \delta_{\alpha, \beta}]. \quad (\text{B3})$$

Similarly the redefinitions of the coefficients appearing in Eqs. (7) and (8) for the higher-order terms are

$$\begin{aligned}
A_{n,m}^{(3)}(k) &= -\frac{1}{4}\sqrt{\frac{S}{2N'}}\left[\left\{\sum_{p=1}^N\sum_{\alpha,\beta}\chi_{n,p}^{\alpha\beta}(0)(P_n^\alpha Q_p^\beta + P_n^\beta Q_p^\alpha) - \frac{g\mu_B H_0}{S}P_n^z\right\}\delta_{n,m}\right. \\
&\quad \left.+ 4\sum_{\alpha,\beta}\chi_{n,m}^{\alpha\beta}(k)(P_n^\alpha Q_m^\beta + P_n^\beta Q_m^\alpha)\right], \\
B_{n,m}^{(3)}(k) &= -\frac{1}{4}\sqrt{\frac{S}{2N'}}\left[\left\{\sum_{p=1}^N\sum_{\alpha,\beta}\chi_{n,p}^{\alpha\beta}(0)[(P_n^\alpha)^* Q_p^\beta + (P_n^\beta)^* Q_p^\alpha] - \frac{g\mu_B H_0}{S}(P_n^z)^*\right\}\delta_{n,m}\right. \\
&\quad \left.+ 4\sum_{\alpha,\beta}\chi_{n,m}^{\alpha\beta}(k)\{Q_n^\alpha (P_m^\beta)^* + Q_n^\beta (P_m^\alpha)^*\}\right], \tag{B4}
\end{aligned}$$

$$A_{n,m}^{(4)}(k) = -\frac{1}{8N'}\sum_{\alpha,\beta}\chi_{n,m}^{\alpha\beta}(k)\{P_n^\alpha (P_m^\beta)^* + P_n^\beta (P_m^\alpha)^*\},$$

$$B_{n,m}^{(4)}(k) = \frac{1}{N'}\sum_{\alpha,\beta}\chi_{n,m}^{\alpha\beta}(k)Q_n^\alpha Q_m^\beta,$$

$$C_{n,m}^{(4)}(k) = -\frac{1}{8N'}\sum_{\alpha,\beta}\chi_{n,m}^{\alpha\beta}(k)\{P_n^\alpha P_m^\beta + P_n^\beta P_m^\alpha\}. \tag{B5}$$

¹*Spin Dynamics in Confined Magnetic Structures I*, edited by B. Hillebrands and K. Ounadjela (Springer, Berlin, 2002).

²*Ultrathin Magnetic Structures III: Fundamentals of Nanomagnetism*, edited by J. A. C. Bland and B. Heinrich (Springer, Berlin, 2005).

³*Ultrathin Magnetic Structures IV: Applications of Nanomagnetism*, edited by B. Heinrich and J. A. C. Bland (Springer, Berlin, 2005).

⁴C. Mathieu, J. Jorzick, A. Frank, S. O. Demokritov, A. N. Slavin, B. Hillebrands, B. Bartenlian, C. Chappert, D. Decanini, F. Rousseaux, and E. Cambril, *Phys. Rev. Lett.* **81**, 3968 (1998).

⁵J. Jorzick, S. O. Demokritov, B. Hillebrands, M. Bailleul, C. Fermon, K. Y. Guslienko, A. N. Slavin, D. V. Berkov, and N. L. Gorn, *Phys. Rev. Lett.* **88**, 047204 (2002).

⁶G. Gubbiotti, S. Tacchi, G. Carlotti, P. Vavassori, N. Singh, S. Goolaup, A. O. Adeyeye, A. Stashkevich, and M. Kostylev, *Phys. Rev. B* **72**, 224413 (2005).

⁷T. M. Nguyen, M. G. Cottam, H. Y. Liu, Z. K. Wang, S. C. Ng, M. H. Kuok, D. J. Lockwood, K. Nielsch, and U. Gösele, *Phys. Rev. B* **73**, 140402(R) (2006).

⁸Z. K. Wang, V. L. Zhang, H. S. Lim, S. C. Ng, M. H. Kuok, S. Jain, and A. O. Adeyeye, *Appl. Phys. Lett.* **94**, 083112 (2009).

⁹J. P. Park, P. Eames, D. M. Engebretson, J. Berezovsky, and P. A. Crowell, *Phys. Rev. Lett.* **89**, 277201 (2002).

¹⁰C. Bayer, J. P. Park, H. Wang, M. Yan, C. E. Campbell, and P. A. Crowell, *Phys. Rev. B* **69**, 134401 (2004).

¹¹C. T. Boone, J. A. Katine, J. R. Childress, V. Tiberkevich, A. Slavin, J. Zhu, X. Cheng, and I. N. Krivorotov, *Phys. Rev. Lett.* **103**, 167601 (2009).

¹²*Spin Dynamics in Confined Magnetic Structures III*, edited by B. Hillebrands and A. Thiaville (Springer, Berlin, 2006).

¹³K. Yu. Guslienko and A. N. Slavin, *Phys. Rev. B* **72**, 014463 (2005).

¹⁴T. M. Nguyen and M. G. Cottam, *Phys. Rev. B* **71**, 094406 (2005).

¹⁵H. T. Nguyen, T. M. Nguyen, and M. G. Cottam, *Phys. Rev. B* **76**, 134413 (2007).

¹⁶F. Keffer, *Handb. Phys.* **18**, 1 (1966).

¹⁷*Spin Waves: Theory and Applications*, D. D. Stancil and A. Prabhakar (Springer, New York, 2009).

¹⁸*Nonlinear Phenomena and Chaos in Magnetic Materials*, edited by P. E. Wigen (World Scientific, Singapore, 1994).

¹⁹*Linear and Nonlinear Spin Waves in Magnetic Films and Superlattices*, edited by M. G. Cottam (World Scientific, Singapore, 1994).

²⁰R. N. Costa Filho, M. G. Cottam, and G. A. Farias, *Phys. Rev. B* **62**, 6545 (2000).

²¹See, e.g., G. Rickayzen, *Green's Functions and Condensed Matter* (Academic Press, London, 1980).

²²K. Yu. Guslienko, V. Pishko, V. Novosad, K. Buchanan, and S. D. Bader, *J. Appl. Phys.* **97**, 10A709 (2005).

²³H. T. Nguyen, G. Gubbiotti, M. Madami, S. Tacchi, and M. G. Cottam, *Microelectron. J.* **40**, 598 (2009).

²⁴M. Kostylev, J.-G. Hu, and R. L. Stamps, *Appl. Phys. Lett.* **90**, 012507 (2007).

²⁵V. V. Kruglyak, S. O. Demokritov, and D. Grundler, *J. Phys. D* **43**, 264001 (2010).